Title

Notch Fracture Toughness of Glasses: Dependence on Rate, Age, and Geometry

Journal

Physical Review Applied, 6(2)

ISSN

2331-7043

Authors

Vasoya, Manish

Rycroft, Chris H

Bouchbinder, Eran

Publication Date

2016-08-01

DOI

10.1103/physrevapplied.6.024008

Peer reviewed

Notch Fracture Toughness of Glasses: Dependence on Rate, Age, and Geometry

Manish Vasoya,[1] Chris H. Rycroft,[2,3] and Eran Bouchbinder[1]
[1]Chemical Physics Department, Weizmann Institute of Science, Rehovot 7610001, Israel
[2]Paulson School of Engineering and Applied Sciences, Harvard University, Cambridge, Massachusetts 02138, USA
[3]Department of Mathematics, Lawrence Berkeley Laboratory, Berkeley, California 94720, USA
(Received 9 April 2016; revised manuscript received 21 June 2016; published 11 August 2016)

Understanding the fracture toughness (resistance) of glasses is a fundamental problem of prime theoretical and practical importance. Here we theoretically study its dependence on the loading rate, the age (history) of the glass, and the notch radius ρ. Reduced-dimensionality analysis suggests that the notch fracture toughness results from a competition between the initial, age- and history-dependent, plastic relaxation time scale $\tau_0^{\rm pl}$ and an effective loading time scale $\tau^{\rm ext}(\dot{K}_I,\rho)$, where $\dot{K}_I$ is the tensile stress-intensity-factor rate. The toughness is predicted to scale with $\sqrt{\rho}$ independently of $\xi \equiv \tau^{\rm ext}/\tau_0^{\rm pl}$ for $\xi \ll 1$, to scale as $T\sqrt{\rho}\log(\xi)$ for $\xi \gg 1$ (related to thermal activation, where T is the temperature), and to feature a nonmonotonic behavior in the crossover region $\xi \sim \mathcal{O}(1)$ (related to plastic yielding dynamics). These predictions are verified using 2D computations, providing a unified picture of the notch fracture toughness of glasses. The theory highlights the importance of time-scale competition and far-from-steady-state elasto-viscoplastic dynamics for understanding the toughness and shows that the latter varies quite significantly with the glass age (history) and applied loading rate. Experimental support for bulk metallic glasses is presented, and possible implications for applications are discussed.

DOI: 10.1103/PhysRevApplied.6.024008

I. INTRODUCTION

The fracture toughness, i.e., the ability to resist failure in the presence of a crack, is a basic physical property of materials [1]. From a practical perspective, this property is a major limiting factor in the structural integrity of a broad range of systems and engineering applications. From a theoretical perspective, the fracture toughness challenges our understanding of the strongly nonlinear and dissipative response of materials under extreme conditions, approaching catastrophic failure. Consequently, obtaining a basic understanding of the fracture toughness of materials is a fundamentally important problem.

Quantitatively predicting the fracture toughness of glassy materials, which lack long-range crystalline order and are characterized by intrinsic disorder, is a particularly pressing problem in condensed-matter, materials, and applied physics. Glassy materials exhibit unique and intriguing physical properties as compared to their crystalline counterparts [2–10]. For example, glassy solids typically exhibit a strength and an elastic limit that significantly exceed those of crystalline alloys of similar composition due to the absence of mobile dislocation defects. Instead, glassy solids deform irreversibly by immobile and localized structural rearrangements [11–13], at sites termed shear-transformation zones (STZs), which are not yet fully understood.

Glassy materials are intrinsically out of equilibrium; hence, their physical properties depend on their preparation protocol, history, and age (see, for example, Refs. [14,15]). Moreover, these materials typically do not feature strain hardening, i.e., an increase in the deformation resistance with increasing deformation, which is commonly observed in crystalline alloys [2–10]. Finally, glassy materials feature rate effects that are far from understood [2–10].

In the past few decades, significant improvement in the glass-forming ability (GFA) of multicomponent amorphous alloys has been achieved, allowing the use of conventional casting techniques to obtain amorphous alloys in bulk forms, the so-called bulk metallic glasses (BMGs) [16–22]. The emergence of this new family of glasses has triggered intense research activity and holds great promise for a wide range of functional and structural engineering applications [2–10]. The reason for this is twofold. First, BMGs are exceptionally strong and elastic compared to conventional engineering materials and exhibit other appealing mechanical and magnetic properties (such as good wear strength, corrosion resistance, and hard-magnetic properties at room temperature). Second, BMGs can be processed as plastics into near-net shapes that are impossible to achieve using conventional metals, due to stable viscous flow in a wide supercooled-liquid region and minute shrinkage at the glass transition [16–22].

A major stumbling block for the widespread usage of BMGs as structural engineering materials in load-bearing applications is their limited ductility and typically low fracture toughness. This severe limitation triggered an extensive search for improving the toughness of BMGs by either exploring new alloys and compositions with

excellent GFA and physical properties or by manipulating existing alloys [3–10]. Unfortunately, this search is not yet based on well-established theoretical predictions but rather on trial-and-error procedures and phenomenological correlations between various physical properties [3–10]. For example, a large body of work focuses on some phenomenological correlations between the elastic moduli of BMGs and important properties such as their fracture toughness and GFA [3–10]. It is highly desirable to put these efforts on solid theoretical grounds which will enhance the predictability of the fracture toughness of glasses and hence pave the way to a broader range of engineering applications.

This challenge has attracted considerable attention and triggered much recent work [23–54]. Yet, there is no complete understanding of the resistance of glassy materials to catastrophic failure in the presence of a notch defect—the notch fracture toughness—and its dependence on various physical parameters. Our goal in this paper is to offer a comprehensive theoretical picture of the dependence of the notch fracture toughness of glasses on the loading rate, the glass age and history, the notch radius, and the temperature (below the glass transition temperature).

Our main result, obtained through a reduced-dimensionality theoretical analysis and extensive 2D spatiotemporal computations based on a recently developed numerical method [55], highlights the essential role played by time-scale competition in determining the notch fracture toughness of glassy materials. The competing time scales involve an effective applied loading time scale (depending on the notch radius of curvature and on the global geometry and loading rate) and the initial, age-dependent, plastic (dissipative) relaxation time scale (depending on the glass cooling rate, age, and history) [56]. Once properly identified, the ratio of the two time scales ξ is shown to control the fracture toughness over a wide range of physical conditions. A master curve describing the dependence of the toughness on ξ is quantitatively derived and is shown to feature a *nonmonotonic* behavior.

These results are shown to be consistent with previously unexplained experimental data and offer various predictions. The theory suggests a way to predict the variation of the notch fracture toughness of glasses over a broad range of physical conditions based on relatively few measurements. It also delineates the range of physical parameters where BMGs could be manipulated, e.g., by controlled heat treatments, to achieve improved toughness for engineering applications. In particular, the minimum of the toughness master curve in terms of ξ is an important rate-dependent material parameter that can guide toughening strategies (e.g., by manipulating the preparation procedure) and put on more solid ground the related phenomenological criteria [51]. Moreover, the theory suggests that phenomenological correlations between elastic moduli and toughness may be somewhat superficial and of limited predictive power. Finally, this work offers tools to quantify the rate dependence of the toughness, which is essential for using BMGs in future load-bearing engineering applications.

II. PROBLEM FORMULATION

The fracture toughness quantifies the amount of dissipation involved in crack propagation. Consequently, one needs to account for the irreversible deformation of the material and its interplay with reversible (elastic) deformation. Inertia plays little role in fracture *initiation* under a wide range of conditions and standard engineering testing protocols; hence, we focus on the quasistatic stress equilibrium described by

$$\nabla \cdot \boldsymbol{\sigma} = \mathbf{0}, \tag{1}$$

where $\boldsymbol{\sigma}$ is the Cauchy stress tensor. We consider then a general hypo-elasto-viscoplastic material described by

$$\boldsymbol{D}^{\mathrm{tot}}(\boldsymbol{v}) = \boldsymbol{D}^{\mathrm{el}}(\boldsymbol{\sigma}, \boldsymbol{v}) + \boldsymbol{D}^{\mathrm{pl}}(\boldsymbol{\sigma}, \ldots). \tag{2}$$

Here $\boldsymbol{D}^{\mathrm{tot}} = \frac{1}{2}[\nabla \boldsymbol{v} + (\nabla \boldsymbol{v})^T]$ is the total rate-of-deformation tensor, where $\boldsymbol{v}(\boldsymbol{r}, t)$ is the Eulerian velocity field and $(\boldsymbol{r}, t)$ are the spatiotemporal coordinates. $\boldsymbol{D}^{\mathrm{el}} = \partial_t \boldsymbol{\epsilon} + \boldsymbol{v} \cdot \nabla \boldsymbol{\epsilon} + \boldsymbol{\epsilon} \cdot \boldsymbol{\omega} - \boldsymbol{\omega} \cdot \boldsymbol{\epsilon}$ is the elastic rate-of-deformation tensor, where $\boldsymbol{\omega} = \frac{1}{2}[\nabla \boldsymbol{v} - (\nabla \boldsymbol{v})^T]$ is the spin tensor and the strain tensor $\boldsymbol{\epsilon}$ is related to $\boldsymbol{\sigma}$ through Hooke's law $\boldsymbol{\sigma} = K \operatorname{tr} \boldsymbol{\epsilon} \boldsymbol{1} + 2\mu(\boldsymbol{\epsilon} - \frac{1}{3} \operatorname{tr} \boldsymbol{\epsilon} \boldsymbol{1})$. K and μ are the bulk and shear moduli, respectively. $\boldsymbol{D}^{\mathrm{pl}}(\boldsymbol{\sigma}, \ldots)$ is the plastic rate-of-deformation tensor, which encapsulates the relevant physics of the dissipative deformation of glasses. The ellipsis stands for additional dependencies, e.g., on the temperature and on structural internal state variables.

We adopt the nonequilibrium thermodynamic STZ model, as in Ref. [35], where

$$\boldsymbol{D}^{\mathrm{pl}}(\boldsymbol{s}, T, \chi) = e^{-(e_z/k_B\chi)} \frac{\mathcal{C}(\bar{s}, T)}{\tau} \left[1 - \frac{s_y}{\bar{s}}\right] \frac{\boldsymbol{s}}{\bar{s}}, \tag{3}$$

$$c_0 \dot{\chi} = \frac{\boldsymbol{D}^{\mathrm{pl}} : \boldsymbol{s}}{s_y} (\chi_\infty - \chi) \tag{4}$$

for $\bar{s} \geq s_y$ and $\boldsymbol{D}^{\mathrm{pl}} = 0$ otherwise. This model, despite its relative simplicity, is shown to capture a wide range of driven glassy phenomena [13,35,57–70]. $\boldsymbol{s} = \boldsymbol{\sigma} - \frac{1}{3} \operatorname{tr} \boldsymbol{\sigma} \mathbf{1}$ in Eqs. (3) and (4) is the deviatoric stress tensor, its magnitude is $\bar{s} \equiv \sqrt{\boldsymbol{s} : \boldsymbol{s}/2}$, and s_y is the shear yield stress. χ is an effective disorder temperature which quantifies the intrinsic structural state of the glass [57,63], e_z/k_B is a typical STZ formation energy over Boltzmann's constant, and $\mathcal{C}(\bar{s}, T)/\tau$ is the rate at which STZs make transitions between their internal states. τ^{-1} is a molecular vibration rate, and T is the bath temperature, assumed to be well below the glass

temperature [such that spontaneous aging is neglected in Eq. (4)]. c_0 is an effective dimensionless heat capacity, and χ_∞ is the steady-state value of χ.

The STZ transition rate is taken to be of the form

$$\mathcal{C}(\bar{s},T)=\begin{cases} e^{-(\Delta/k_BT)}\cosh\left[\frac{\Omega\epsilon_0\bar{s}}{k_BT}\right] & \text{for } \Omega\epsilon_0\bar{s}<\Delta, \\ \frac{\Omega\epsilon_0\bar{s}}{2\Delta} & \text{for } \Omega\epsilon_0\bar{s}\geq\Delta. \end{cases} \quad (5)$$

It corresponds to a linearly stress-biased thermal activation process at relatively small stresses, where Δ is the typical energy activation barrier, Ω is the typical activation volume, and ϵ_0 is the typical local STZ strain. In the presence of the high stresses near a tip of a crack, $\Omega\epsilon_0\bar{s}$ may become larger than Δ, in which case we assume that the exponential thermal activation form crosses over to a much weaker dependence associated with a linear, nonactivated, dissipative mechanism [61]. As $\Delta\gg k_BT$, the two regimes connect continuously but not differentiably. This crossover in the form of the STZ transition rates, from exponential thermal activation to a much weaker athermal power law (here a linear relation, which allows for analytic progress), turns out below to have important implications for the toughness.

This elasto-viscoplasticity model is used to formulate a plane-strain fracture problem where traction-free boundary conditions are imposed on a blunted straight notch (crack) with an initial root radius ρ (cf. Fig. 1) and the universal linear elastic mode-I (tensile) crack tip velocity fields [71]

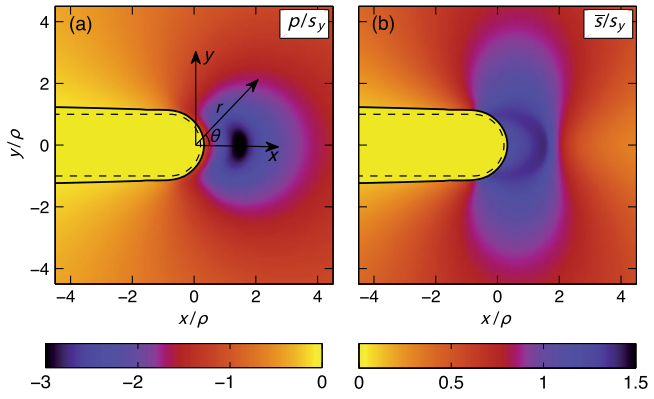

FIG. 1. The problem setting and an example of a numerical solution in the near-notch-root region. (a) The hydrostatic pressure and (b) the magnitude of the deviatoric stress, both normalized by the shear yield stress s_y, are shown. The dashed-dotted line corresponds to the initial notch state and the solid line to a deformed state with $K_I=30$ MPa$\sqrt{\text{m}}$. A small portion of the simulation domain $-20\leq x/\rho, y/\rho\leq 20$, near the notch root, is shown. A fixed coordinate system located a distance $\rho/5$ behind the initial notch root, with both Cartesian (x,y) and polar (r,θ) coordinates, is shown in (a). The calculation is done using a 1025×1025 grid.

$$\boldsymbol{v}(r,\theta,t)=\frac{\dot{K}_I(t)}{\mu}\sqrt{\frac{r}{2\pi}}\boldsymbol{F}(\theta)\quad\text{for } r\gg\rho \quad (6)$$

are imposed on a scale much larger than ρ. Here $\dot{K}_I$ is the mode-I stress-intensity-factor rate, which measures the intensity of the linear elastic singularity $\nabla\boldsymbol{v}\sim 1/\sqrt{2\pi r}$ at $\rho\ll r\ll L$, where L is a macroscopic length scale in the global fracture problem (e.g., the sample size). (r,θ) is a polar coordinate system whose origin is set a distance $\rho/5$ behind the notch root, $\theta=0$ is the symmetry axis, and $\boldsymbol{F}(\theta)$ is a known universal function [35,71]. In such a boundary layer formulation, the stress-intensity factor uniquely couples the inner scales near the notch root to the outer scales and, hence, can be controlled independently without solving the global fracture problem [71].

The notch fracture toughness is the critical value of the stress-intensity factor, K_Q, at which crack propagation initiates and global failure occurs. Recent work [35,40–49] suggests that this onset (and in fact also the subsequent propagation [35]) is controlled by a local cavitation instability occurring when the hydrostatic tension $\frac{1}{3}\text{tr}\boldsymbol{\sigma}$ surpasses a threshold level σ_c. We adopt this failure criterion here.

While a large part of the analysis below is performed in terms of dimensionless parameters, we nevertheless consider realistic material parameters corresponding to Vitreloy 1, a widely studied BMG, identical to those reported in Ref. [35]. That is, we use $T=400$ K, $e_z/k_B=21\,000$ K, $s_y=0.85$ GPa, $\mu=37$ GPa, $K=122$ GPa, $\tau=10^{-13}$ s, $\epsilon_0=0.3$, $\Omega=300$ Å^3, $c_0=0.4$, $\Delta/k_B=8000$ K, and $\chi_\infty=900$ K. For the initial conditions, we use $\boldsymbol{\sigma}(\boldsymbol{r},t=0)=0$ and $\chi(\boldsymbol{r},t=0)=\chi_0$, where χ_0 describes the initial structural state of the glass which depends on its history. For example, it may be affected by the cooling rate at which the glass has been formed, annealing and other heat treatments, aging time, and previous deformation. The model's setup is shown in Fig. 1.

III. THEORY AND ANALYSIS

Our major goal is to study the dependence of the notch fracture toughness K_Q on the initial structural state of the glass χ_0, on the stress-intensity-factor rate $\dot{K}_I$, on the notch radius of curvature ρ, and on the temperature T below the glass transition temperature. We address the problem of calculating $K_Q(\chi_0,\dot{K}_I,\rho,T)$ by a reduced-dimensionality theoretical analysis and 2D numerical computations. The latter, an example of which is shown in Fig. 1, are based on a recently developed numerical method that can handle physically realistic loading rates, which is essential for understanding the properties of the toughness. Preliminary numerical results addressing this problem appeared in Ref. [35].

To gain some analytic insight into the fracture toughness, we perform a reduced-dimensionality analysis which aims at describing the behavior of a representative material element near the notch root. We further simplify the problem by eliminating its tensorial nature, focusing only on the magnitude of the deviatoric component of the relevant tensors. In particular, we neglect altogether the hydrostatic part of the stress tensor $\boldsymbol{\sigma}$ and replace its deviatoric part $\boldsymbol{s}(\boldsymbol{r},t)$ by a space-independent scalar $s(t)$ and $\chi(\boldsymbol{r},t)$ by $\chi(t)$. Similarly, we replace the space-dependent elastic and plastic rate-of-deformation tensors in the problem by their space-independent scalar counterparts $\boldsymbol{D}^{\mathrm{el}}(\boldsymbol{r},t)\to\dot{s}(t)/\mu$ and $\boldsymbol{D}^{\mathrm{pl}}(\boldsymbol{r},t)\to D^{\mathrm{pl}}(t)$, with $D^{\mathrm{pl}}(s,\chi)=\tau^{-1}e^{-(e_z/k_B\chi)}\mathcal{C}(s,T)(1-s_y/s)$.

The crucial last step is to relate the global loading and geometry of the system, captured by the stress-intensity factor K_I, and the effective total rate of deformation near the notch root, taking into account both the strong stress amplification associated with the linear elastic square-root singularity and the characteristic length scale inherited from the notch radius of curvature. A natural way to do this is through the replacement

$$\boldsymbol{D}^{\mathrm{tot}}(\boldsymbol{r},t)\to\frac{\dot{K}_I}{\mu\sqrt{2\pi\rho}}. \tag{7}$$

With these replacements, Eqs. (3) and (4) transform into a set of coupled nonlinear ordinary differential equations:

$$\dot{s}=\frac{\dot{K}_I}{\sqrt{2\pi\rho}}-\mu D^{\mathrm{pl}}(s,\chi), \tag{8}$$

$$c_0\dot{\chi}=\frac{D^{\mathrm{pl}}(s,\chi)s}{s_y}(\chi_\infty-\chi). \tag{9}$$

Obviously, Eqs. (8) and (9) miss many features of the full $(2+1)$-dimensional spatiotemporal dynamics of the problem, such as the tensorial nature of the basic quantities, the coupling between the deviatoric and hydrostatic parts of the deformation and stress, the time evolution of the radius of curvature $\rho(t)$, and the propagation of yielding fronts in the notch-root region. Yet, as shown below, they capture important aspects of the fracture toughness. The first step in analyzing Eqs. (8) and (9) is to identify a proper set of dimensionless physical parameters that control their behavior. In this context, we stress that elasto-viscoplasticity is intrinsically linked to a competition between different time scales. Moreover, glassy response is sensitive to the *initial* structural state of the material (affected by its age, cooling rate, previous deformation, etc.), which must play a crucial role in far-from-steady-state physical properties such as the fracture toughness.

To capture this time-scale competition, we define an *initial* plastic relaxation time scale (inverse rate) as $\tau_0^{\mathrm{pl}}(\chi_0)\equiv\tau e^{(e_z/k_B\chi_0)}$, an effective applied time scale (again, an inverse rate) as $\tau^{\mathrm{ext}}(\dot{K}_I,\rho)\equiv\mu\sqrt{2\pi\rho}/\dot{K}_I$, and their ratio as

$$\xi(\chi_0,\dot{K}_I,\rho)\equiv\frac{\tau^{\mathrm{ext}}}{\tau_0^{\mathrm{pl}}}=\frac{\mu\sqrt{2\pi\rho}}{\tau\dot{K}_I}e^{-(e_z/k_B\chi_0)}. \tag{10}$$

This dimensionless quantity plays a central role in what follows. It is important to note that $1/\tau^{\mathrm{ext}}$ is *not* the externally applied strain rate but rather the effective strain rate experienced by the near-notch region. The effective strain rate at the innermost scale $r\simeq\rho$ is significantly amplified relative to the externally applied strain rate, characterizing the outermost scale L, according to the linear elastic square-root singularity.

We also define $\tilde{e}_z\equiv e_z/k_B\chi_0$, $\tilde{\chi}_\infty\equiv\chi_\infty/\chi_0$, $\tilde{\mu}\equiv\mu c_0/s_y$, $\tilde{s}\equiv s/s_y$, $\tilde{\chi}\equiv\chi/\chi_0$, and $\tilde{t}\equiv t\dot{K}_I/s_y\sqrt{2\pi\rho}$. In terms of these dimensionless quantities, Eqs. (8) and (9) take the form

$$\dot{\tilde{s}}=1-\xi f(\tilde{s},\tilde{\chi}), \tag{11}$$

$$\tilde{\mu}\dot{\tilde{\chi}}=\xi f(\tilde{s},\tilde{\chi})\tilde{s}(\tilde{\chi}_\infty-\tilde{\chi}), \tag{12}$$

with $f(\tilde{s},\tilde{\chi})\equiv e^{\tilde{e}_z(1-\tilde{\chi}^{-1})}\mathcal{C}(s,T)(1-\tilde{s}^{-1})$ for $\tilde{s}\geq 1$ (for $\tilde{s}<1$, we have $f=0$). It should be noted that nondimensionalizing differential equations using an initial condition, in our case χ_0, might appear unnatural. Yet, it is a choice that is dictated by the physics of glasses, which exhibit a rather unique dependence on the initial state.

To proceed, we distinguish between two regimes: one in which the deviatoric stress significantly surpasses $\Delta/\Omega\epsilon_0$, where $\mathcal{C}\sim s$, and one in which the deviatoric stress remains close to $\Delta/\Omega\epsilon_0$, where $\mathcal{C}$ varies exponentially with the stress [cf. Eq. (5)]. We focus first on the former and for the sake of simplicity set $2\Delta/\Omega\epsilon_0=s_y$, which means that we exclude thermal activation altogether in this part of the reduced-dimensionality analysis.

In Figs. 2(a) and 2(b), we present $\tilde{s}(\tilde{t})$ and $\tilde{\chi}(\tilde{t})$ for two values of ξ which differ by an order of magnitude. It is observed that as ξ decreases, when τ^{ext} decreases relative to τ_0^{pl}, the yielding behavior of the material (i.e., the transition from elastic-dominated to plastic-dominated deformation) changes quite significantly. In particular, an elastic overshoot leads to a significant increase in the peak stress $\tilde{s}_p$ with decreasing ξ, and the subsequent dynamics exhibit a sharp drop in the stress $\tilde{s}$ and a sharp increase in the effective temperature $\tilde{\chi}$. These sharp postyielding dynamics mark the emergence of a short time scale associated with a strongly nonlinear material response.

Our next goal is to better understand this behavior and its relation to the fracture toughness. To that aim, we first try to estimate the peak stress $\tilde{s}_p$, for which $\dot{\tilde{s}}=0$. The latter translates into the relation $e^{\tilde{e}_z(1-\tilde{\chi}_p^{-1})}(\tilde{s}_p-1)=\xi^{-1}$ between

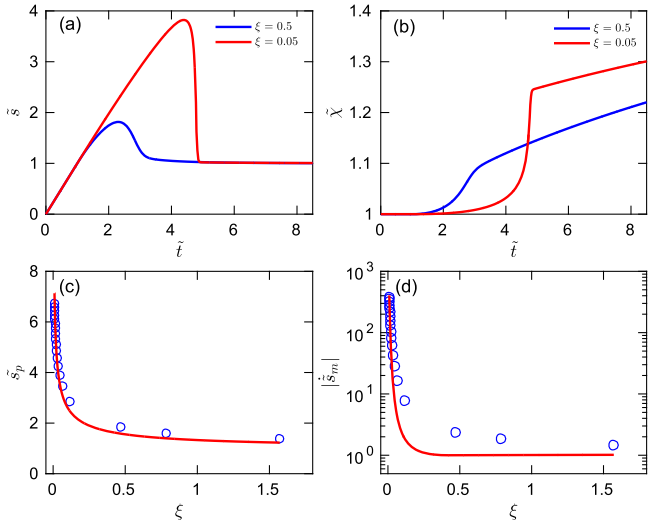

FIG. 2. The solution of Eqs. (11) and (12), for two values of ξ (separated by an order of magnitude). The stress is shown in (a) and the effective temperature in (b). We use $\tilde{\mu} = 15.07$, $\tilde{e}_z = 35$, $\tilde{\chi}_\infty = 1.5$, and $\mathcal{C} = \tilde{s}$, with the initial conditions $\tilde{s}(0) = 0$ and $\tilde{\chi}(0) = 1$. (c) The analytic prediction for the peak stress $\tilde{s}_p$ in Eq. (13) (solid red line) compared to the peak stress obtained from a numerical solution of Eqs. (11) and (12) (open blue circles). (d) The prediction of the maximal stress drop rate $|\dot{\tilde{s}}_m|$ in the postpeak regime following Eq. (14) (solid red line) compared to the maximal stress drop rate obtained from a numerical solution of Eqs. (11) and (12) (open blue circles).

$\tilde{s}_p$ and $\tilde{\chi}_p \equiv \tilde{\chi}(\tilde{s}_p)$. An approximate solution for the stress peak can be derived in the form

$$\tilde{s}_p \simeq 1 - \frac{\zeta + \tilde{\mu}}{4\zeta} + \frac{\sqrt{8\zeta\tilde{\mu}\xi^{-1} + (\zeta + \tilde{\mu})^2}}{4\zeta}, \qquad (13)$$

with $\zeta \equiv 1 + \tilde{e}_z(\tilde{\chi}_\infty - 1)$. $\tilde{\chi}_p$ is given by the exact relation $\tilde{\chi}_p(\tilde{s}_p) = \{1 + \tilde{e}_z^{-1}\log[\xi(\tilde{s}_p - 1)]\}^{-1}$. In Fig. 2(c), we compare the analytic estimation in Eq. (13) to the peak stress obtained from the full numerical solution of Eqs. (11) and (12). It is observed that the analytic approximation accurately captures the increase in $\tilde{s}_p$ with decreasing ξ. In light of the latter, we expect $\tilde{\chi}_p(\tilde{s}_p)$ given above to yield good approximations as well, which is indeed the case (not shown).

With $\tilde{s}_p$ and $\tilde{\chi}_p$ at hand, we can estimate the stress drop rate in the postpeak dynamics, observed in Fig. 2(a). As the plastic rate of deformation is strongly amplified during the drop, we neglect the external loading term $\dot{K}_I/\sqrt{2\pi\rho}$ in Eq. (8). With this approximation, which is expected to be valid for small ξ, we can eliminate $D^{\mathrm{pl}}(s,\chi)$ between Eqs. (8) and (9), obtaining a differential equation for $\chi(s)$ (i.e., time becomes a parameter). The solution, which is expected to be valid deep inside the stress drop region, takes the form $\tilde{\chi}(\tilde{s}) \simeq \tilde{\chi}_\infty - (\tilde{\chi}_\infty - \tilde{\chi}_p)\exp[(\tilde{s}^2 - \tilde{s}_p^2)/(2\tilde{\mu})]$. Using the latter, we obtain the following estimate:

$$\dot{\tilde{s}}(\tilde{s}) \simeq -\xi e^{\tilde{e}_z[1-\tilde{\chi}(\tilde{s})^{-1}]}(\tilde{s} - 1) \qquad (14)$$

for the stress rate during the drop, which should be valid for $1 < \tilde{s} < \tilde{s}_p$, not too close to either 1 or $\tilde{s}_p$.

It is important to note that $\tilde{\chi}(\tilde{s})$ in Eq. (14) depends on ξ also through $\tilde{s}_p$ and $\tilde{\chi}_p(\tilde{s}_p)$, which give rise to a super-exponential increase in the maximal value of $\dot{\tilde{s}}(\tilde{s})$, $|\dot{\tilde{s}}_m|$, with decreasing ξ. The prediction in Eq. (14) is compared to the full solution in Fig. 2(d), demonstrating reasonable agreement at small values of ξ, where it is expected to be valid. Note that $|\dot{\tilde{s}}_m|$ in Fig. 2(d) is 1–2 orders of magnitude larger than the effective external loading rate [which is unity in the dimensionless form; cf. Eq. (11)] for sufficiently small ξ, as assumed before. This analysis shows how nonlinear yielding in glassy materials can dynamically generate new, and much shorter, time scales.

In order to understand the implications of this reduced-dimensionality analysis on the toughness, we need to consider spatial interactions between different material elements and the coupling between the deviatoric and the hydrostatic components of the stress tensor. Both components obviously increase linearly with increasing K_I in the elastic regime. When a material element with the largest deviatoric stress yields, the stress is redistributed to nearby material elements. In particular, when ξ is small and a sharp deviatoric stress drop accompanies yielding as shown in Fig. 2(a), nearby material elements experience a *sharp increase* in stress, and hence the maximal stress increases abruptly. This applies to both the deviatoric $\boldsymbol{s}$ and the hydrostatic $\frac{1}{3}\mathrm{tr}\boldsymbol{\sigma}$ components of the stress tensor $\boldsymbol{\sigma}$, which are coupled through the stress equilibrium equation $\nabla \cdot \boldsymbol{\sigma} = \mathbf{0}$. To show this, we plot in Fig. 3(a) the maximum (in space) of the magnitude of the deviatoric stress $\boldsymbol{s}$, $\bar{s}_m$, and of the hydrostatic tension $\frac{1}{3}\mathrm{tr}\,\boldsymbol{\sigma} \equiv -p$, $|p|_m$, obtained from a numerical solution of the full $(2+1)$-dimensional problem with $\chi_0 = 595$ K and $\dot{K}_I = 25$ MPa$\sqrt{\mathrm{m}}$/s (corresponding to $\xi = 0.14$). We observe that indeed both quantities abruptly increase *together* at a certain applied stress-intensity factor K_I.

If the increase in $|p|_m$ for the given ξ is sufficiently large, it can reach the threshold σ_c, which in our model implies failure (and hence the toughness is determined). Consider then what happens for yet smaller values of ξ, $\xi \ll 1$, corresponding to larger $\dot{K}_I$'s or smaller χ_0's. In this case, we expect the threshold σ_c to be reached within the predominantly elastic regime and hence the toughness to be ξ independent in this regime. This implies that there might be a range of ξ's in which the toughness decreases when ξ increases. That is, this scenario implies that the toughness can vary *nonmonotonically* with ξ. To test this, we plot in Fig. 3(b) $|p|_m$ for $\xi = 0.14$ [exactly as in Fig. 3(a)] and also for $\xi = 4 \times 10^{-3} \ll 1$, along with $\sigma_c = 4.5 s_y$ (horizontal line, the same value as in Ref. [35]). We indeed observe

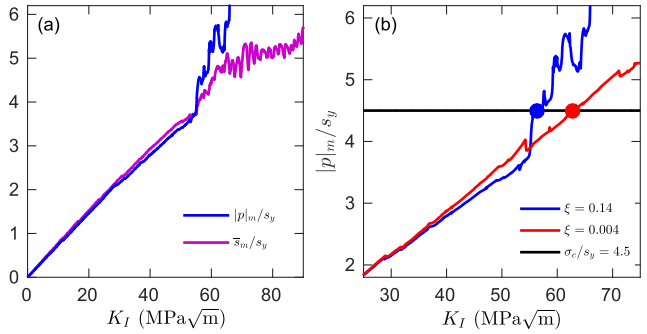

FIG. 3. (a) The maximum (in space) of the hydrostatic tension $|p|_m$ and the magnitude of the deviatoric stress $\bar{s}$ (both in units of s_y) as a function of K_I, obtained from a numerical solution of the full $(2+1)$-dimensional problem with $\chi_0 = 595$ K, $\dot{K}_I = 25$ MPa$\sqrt{\text{m}}$/s, and $\rho = 65$ μm, corresponding to $\xi = 0.14$. It is observed that the two quantities experience an abrupt increase at the same value of K_I. (b) The maximum (in space) of the hydrostatic tension $|p|_m$ (in units of s_y) as a function of K_I, for $\xi = 0.14$ [as in (a)] and $\xi = 4 \times 10^{-3} \ll 1$, together with a cavitation threshold corresponding to $\sigma_c/s_y = 4.5$ (solid black horizontal line). It is observed that, for the larger ξ, the cavitation threshold is exceeded at a smaller K_I, implying a nonmonotonic behavior of the fracture toughness.

that the threshold is reached at a smaller K_I for the larger ξ, i.e., that the fracture toughness is indeed nonmonotonic.

These predictions are tested over a wide range of parameters in Figs. 4(a) and 4(b), where we plot the toughness as a function of $\dot{K}_I$ [Fig. 4(a), for various χ_0's] and χ_0 [Fig. 4(b), for various $\dot{K}_I$'s], as obtained from the full $(2+1)$-dimensional computations. The emergence of a nonmonotonic dependence of the toughness for a large range of parameters is evident, as well as the saturation of the toughness for sufficiently small χ_0 and sufficiently large $\dot{K}_I$ (corresponding to $\xi \ll 1$). The minimum in the toughness shifts systematically with χ_0 and $\dot{K}_I$. Note that, while the nonmonotonicity is not huge in magnitude, of the order of 10 MPa$\sqrt{m}$, it is a distinct and qualitative feature of strongly nonlinear yielding dynamics in our model. Note also that the nonmonotonic behavior disappears for large enough χ_0 [cf. the $\chi_0 = 640$ K curve in Fig. 4(a)] and large enough $\dot{K}_I$ [not shown in Fig. 4(b), it requires yet larger $\dot{K}_I$ values].

Finally, we also plot in Fig. 4(c) the variation of the toughness with ρ (for various χ_0's, with $\dot{K}_I = 20$ MPa$\sqrt{\text{m}}$/s), discussed below. The toughness is obviously a monotonically increasing function of ρ, as increasing the notch radius of curvature implies enhanced plastic dissipation and less stress concentration. Yet the monotonic ρ dependence in Fig. 4(c) is connected below to the nonmonotonic behavior observed in Figs. 4(a) and 4(b) with respect to χ_0 and $\dot{K}_I$.

IV. MAIN RESULT

Up to now, in the analysis of the reduced-dimensionality model in Eqs. (8) and (9), we use $\mathcal{C} \sim s$. This cannot be valid in the large χ_0 and small $\dot{K}_I$ limits (corresponding to large ξ), where stresses remain close to s_y and $\mathcal{C}(\cdot)$ in Eq. (5) is expected to be determined by thermal activation. Consequently, we would like now to gain some insight into the behavior of Eqs. (8) and (9) when $\mathcal{C}(s,T) = e^{-\Delta/k_BT}\cosh[\Omega\epsilon_0 s/k_BT]$. As the stress remains close to s_y, we assume that $\chi \simeq \chi_0$ and expand $\dot{s} = 0$ near s_y. We can then solve for the peak stress, which takes the form $\tilde{s}_p = 1 + \psi^{-1}W(2\psi\xi^{-1}e^{\Delta/k_BT}e^{-\psi})$, where $\psi \equiv (\Omega\epsilon_0 s_y)/(k_BT)$ and $W(\cdot)$ is the Lambert W function. For realistic numbers, the argument of the latter is large, and we have $W(x) \simeq \log(x)$. Consequently, $\tilde{s}_p$ depends on ξ through $T\log\xi$, a clear signature of thermal activation. We *hypothesize* that the toughness K_Q features the same

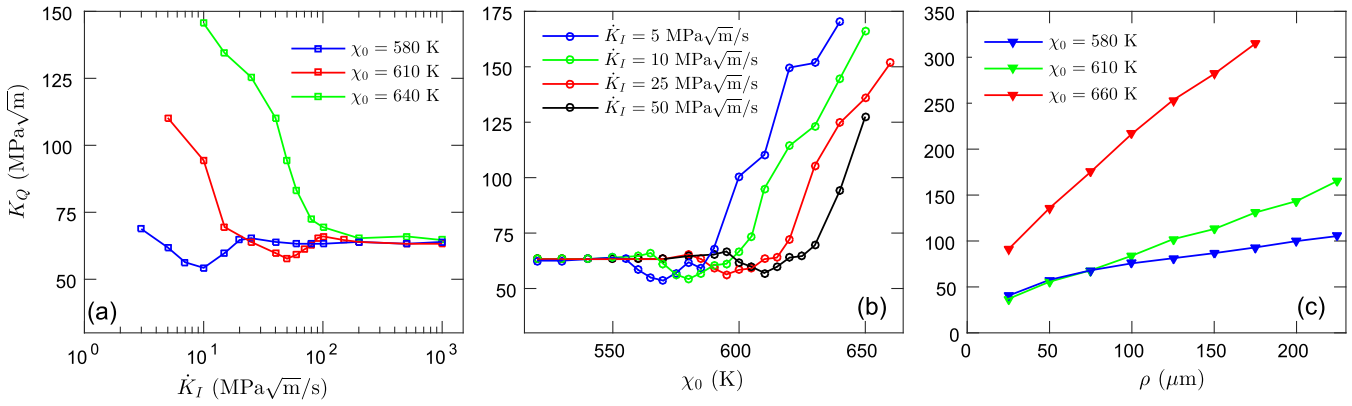

FIG. 4. The notch fracture toughness $K_Q(\chi_0, \dot{K}_I, \rho, T)$ as obtained from numerical solutions of the full $(2+1)$-dimensional problem. (a) K_Q as a function of $\dot{K}_I$ for various χ_0's, with $\rho = 65$ μm and $T = 400$ K. (b) K_Q as a function of the initial structural state χ_0 for various $\dot{K}_I$'s, with $\rho = 65$ μm and $T = 400$ K. (c) K_Q as a function of the notch radius ρ for various χ_0's, with $\dot{K}_I = 20$ MPa$\sqrt{\text{m}}$/s and $T = 400$ K.

dependence when ξ is large, i.e., when stresses remain relatively small.

We are now ready to put all elements of the analysis into a unified prediction for $K_Q(\chi_0, \dot{K}_I, \rho, T)$. The analysis above suggests that the natural quantity to consider is actually $K_Q/\sqrt{\rho}$ (which can be made dimensionless using a stress scale, say, s_y). Consequently, we have

$$\frac{K_Q(\chi_0, \dot{K}_I, \rho, T)}{\sqrt{\rho}} \sim \begin{cases} \text{const} & \text{for } \xi \ll 1, \\ g(\xi) & \text{for } \xi \sim \mathcal{O}(1), \\ T\log(\xi) & \text{for } \xi \gg 1, \end{cases} \quad (15)$$

where $g(\xi)$ features a nonmonotonic behavior for not too large χ_0 and $\dot{K}_I$ [i.e., $g(\xi)$ is not a unique function of ξ for large enough χ_0 and $\dot{K}_I$]. To test this major prediction, we replot in Fig. 5 the data appearing in Fig. 4 as $K_Q/s_y\sqrt{\rho}$ vs ξ in the linear-log scale. We observe that, as predicted, all data collapse onto a single master curve in the $\xi \ll 1$ limit, where it is a constant, and in the $\xi \gg 1$ limit, where it varies as $\log(\xi)$, and feature a nonmonotonic behavior for $\xi \sim \mathcal{O}(1)$ for a broad range of parameters.

Note, in particular, the data corresponding to variations in ρ, which fall onto the nonmonotonic parts of the curve and on the $\log(\xi)$ part. That means that, while K_Q is monotonic in ρ, when the proper dimensionless variables are used, it can reveal the nonmonotonic behavior of the toughness master curve. Furthermore, it implies that the dependence of K_Q on ρ differs from the existing literature, both theoretical and experimental, where K_Q is expected to be either proportional to or linear in $\sqrt{\rho}$, mainly based on dimensional arguments [25,28,29,31,32,36]. While this dependence would give *apparently* reasonable fits to the data in Fig. 4(c), our analysis shows that there exists an *additional* and previously overlooked dependence on ρ through $\xi(\chi_0, \dot{K}_I, \rho)$, for both $\xi \sim \mathcal{O}(1)$ and $\xi \gg 1$.

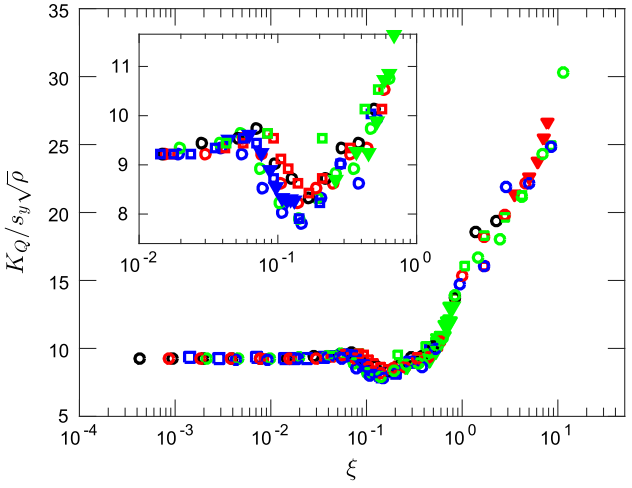

FIG. 5. The dimensionless notch toughness $K_Q(\chi_0, \dot{K}_I, \rho, T)/(s_y\sqrt{\rho})$ as a function of ξ, using all the data presented in Fig. 4. As predicted theoretically in Eq. (15), all data sets (except one in the nonmonotonic part of the curve) collapse on a single master curve being a constant for $\xi \ll 1$, varying as $\log(\xi)$ for $\xi \gg 1$ and featuring a nonmonotonic behavior for $\xi \sim \mathcal{O}(1)$. (Inset) Enlargement of the nonmonotonic part of the toughness master curve. Note in particular that data corresponding to the monotonic variation of the toughness with ρ in Fig. 4(c) nicely collapse on the nonmonotonic part of the master curve (solid triangles) and that one data set (open green squares) does not exhibit a nonmonotonic behavior [corresponding to the $\chi_0 = 640$ K data set in Fig. 4(a)].

It should be stressed that the crossover from the $\xi \ll 1$ behavior to the $\xi \gg 1$ behavior, with the possible nonmonotonicity, is directly related to the change in the transition rate factor $\mathcal{C}$ in Eq. (5) with increasing stress, from thermal activation at relatively small stresses to athermal processes at higher stresses. This change in behavior, which is not commonly discussed in the literature, implies that different parts of the function $K_Q(\chi_0, \dot{K}_I, \rho, T)$ depend differently on the temperature (note, though, that we do not consider other possible dependencies on the temperature). In particular, we verify that the $\log(\xi)$ dependence originates from thermal activation (e.g., it disappears if thermal activation is eliminated altogether, and its logarithmic slope varies in proportion to T), which suggests that glasses exhibit appreciable thermal effects well below their glass temperature. These predictions can be tested by systematically performing notch toughness experiments at different temperatures.

Figure 5, which summarizes our main result, provides a comprehensive picture of the notch toughness of glasses and various testable predictions. It shows that the toughness emerges from a competition between the *initial* (i.e., far-from-steady-state) plastic relaxation time scale, which depends on the glass history and age, and an effective loading time scale near the notch root, which depends on the global problem though $\dot{K}_I$ and on the notch geometry through ρ. It also shows that the notch fracture toughness of glasses can vary quite substantially, as claimed in Ref. [35], by changing ξ. The toughness shown in Figs. 4 and 5 implies a variation of more than an order of magnitude in the fracture energy $\Gamma \propto K_I^2/\mu$ [1].

V. EXPERIMENTAL EVIDENCE

While the toughness of glasses was experimentally studied by various groups, there are relatively few works that systematically vary the stress-intensity-factor rate, the age of the glass, and the notch radius over a large range. In Fig. 6, we show three experimental data sets for BMGs available in the literature, where the notch toughness is measured as a function of $\dot{K}_I$ [Figs. 6(a) and 6(b)] and ρ [Fig. 6(c)].

Inspired by the theoretical prediction in Eq. (15) and its numerical validation in Fig. 5, we replot in

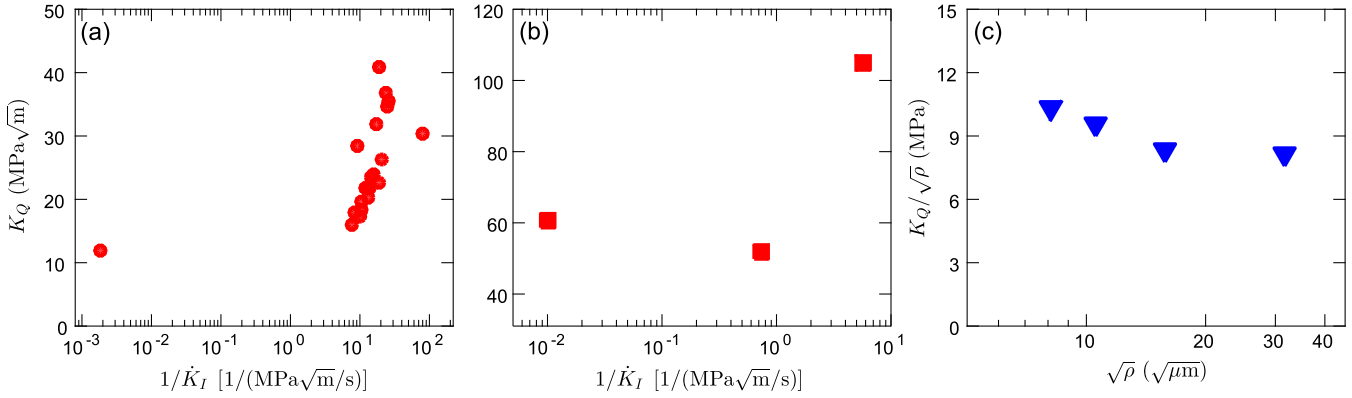

FIG. 6. Experimental support for BMGs. (a) The notch fracture toughness data $K_Q(\dot{K}_I)$ of Ref. [27] replotted as K_Q vs $\log(1/\dot{K}_I)$, following the theoretical prediction in Eq. (15). (b) The same as (a), but for the data of Ref. [28]. (c) The notch fracture toughness data $K_Q(\rho)$ of Ref. [29] replotted as $K_{Ic}/\sqrt{\rho}$ vs $\log(\sqrt{\rho})$, following the theoretical prediction in Eq. (15).

Figs. 6(a) and 6(b) the data of Ref. [27] and of Ref. [28], respectively, as K_Q vs $\log(1/\dot{K}_I)$. The data in Fig. 6(a) are consistent with our predictions, as they feature a quasilogarithmic dependence on $\log(1/\dot{K}_I)$ for small $\dot{K}_I$ and indicate the existence of a plateau for large $\dot{K}_I$'s. There is, however, a gap of nearly 4 orders in magnitude in $\dot{K}_I$ in the data, so the possible nonmonotonic behavior at intermediate $\dot{K}_I$'s cannot be tested. The data in Fig. 6(b) feature all of the predicted trends, including a nonmonotonicity of a similar magnitude compared to our prediction, though there are too few experimental points to test functional dependencies.

In Fig. 6(c), we replot the data of Ref. [29] as $K_Q/\sqrt{\rho}$ vs $\log(\sqrt{\rho})$. The experimental data, where ρ ranges from 65 to 250 μm, seem to be consistent with the decreasing part of the toughness master curve in Fig. 5 and possibly indicate the existence of a minimum. A broader range of ρ's, together with varying also χ_0 and $\dot{K}_I$, are needed in order to test the predicted functional dependencies, but it is already clear that replotting the existing data inspired by to our theory reveals features of the toughness. Our theory certainly calls for additional experiments, as it offers various qualitative and quantitative predictions.

VI. DISCUSSION, IMPLICATIONS FOR APPLICATIONS, AND PROSPECTS

In this paper, we provide a comprehensive theory of the notch fracture toughness of glassy solids, focusing on its dependence on the structural state of the glass (quantified by the initial value of the effective disorder temperature χ_0), on the stress-intensity-factor rate $\dot{K}_I$, on the notch radius of curvature ρ, and on the temperature T below the glass transition temperature. The main results are the theoretical prediction in Eq. (15) and its numerical validation in Fig. 5 based on a computational method [55]. The theory highlights the underlying competition between an intrinsic plastic relaxation time scale and an extrinsic driving time scale, as well as the roles played by nonlinear yielding dynamics and a crossover between thermal and athermal rheological processes. The theoretical predictions are shown to be consistent with existing experimental data.

These results may have implications for the usage of BMGs in load-bearing engineering applications. The master curve in Fig. 5, which features a minimum at $\xi_m \sim \mathcal{O}(1)$, shows that for $\xi \ll \xi_m$ the normalized toughness reaches a low-value plateau, while for $\xi > \xi_m$ it increases as $\log(\xi)$. Since ξ is monotonic in χ_0, this means that, for fixed $\dot{K}_I$ and ρ, varying χ_0 in the range $\xi < \xi_m$ has little effect on the glass (which will be relatively brittle), while increasing χ_0 in the range $\xi > \xi_m$ can significantly enhance the toughness (making the glass more ductile). In the latter regime, we have $K_Q \sim \log(\xi) = \text{const} - [(e_z)/(k_B\chi_0)]$, where typically $e_z \gg k_B\chi_0$. Therefore, small variations of χ_0 in this regime can have a significant effect on the toughness.

The value of χ_0, as stressed above, is affected by the history of the glass, which includes the preparation protocol, the cooling rate, the age of the glass, heat treatments, and previous deformation. For example, by annealing near the glass temperature, χ_0 can be reduced, and if it is in the range $\xi > \xi_m$, it will lead to the annealing-induced embrittlement [23,24,35,38,51]. On the other hand, by increasing the cooling rate by which the BMG is formed (but still resulting in bulk samples) [51,54] and by rejuvenating the glass through a specially designed heat treatment after it is cast (as, for example, recently suggested in Ref. [52]), the glass can be significantly toughened in the range $\xi > \xi_m$. As ξ also incorporates $\dot{K}$, similar effects can be obtained, depending on the typical loading rate relevant for a given device or application.

It is therefore important to identify ξ_m for a given glass and typical performance and external conditions. Related ideas were recently developed in Ref. [51], where the phenomenological notion of a critical fictive temperature is

discussed. In fact, our main result in Fig. 5 bears a resemblance to Fig. 1(a) of Ref. [51], though in the latter only the macroscopic bending strain to failure is measured (and not the fracture toughness itself) and the loading rate is not varied. We believe that the resemblance is well founded and, consequently, that our theoretical results substantiate and significantly expand the results of Ref. [51], making them relevant to various applications.

We also note that, as the elastic moduli are expected to be well-defined functions of χ_0, some correlations between them and the toughness might emerge occasionally. Even when such correlations appear to exist, our results show that they are not causal, i.e., that the elastic moduli do not determine the toughness, but rather that both are affected by χ_0 [35]. In fact, the dependence of the toughness on χ_0 is much stronger and is responsible for the toughness-control opportunities offered in this work. Consequently, we do not expect correlations between elastic moduli and the fracture toughness to offer well-founded predictive tools for the design of improved BMGs for engineering applications.

The analysis presented is based on a simple version of the nonequilibrium thermodynamic STZ model [35]. We suspect that, despite its relative simplicity, the model captures some salient features of glassy rheology that are not specific to the STZ model, which in turn account for generic properties of the notch fracture toughness of glasses. In particular, the model features a competition between internal plastic relaxation rates and externally applied deformation rates, taking into account the universal stress-intensity-factor fields and the notch geometry. Furthermore, the model incorporates a dynamic structural variable (in our case, the effective temperature χ) which accounts for both the dependence on the initial state (cooling rate, history of deformation, etc.) and for the strongly nonlinear strain-softening behavior upon yielding. Finally, the model incorporates thermal activation below the glass transition temperature and a threshold for fracture initiation. We believe that any elastic-viscoplastic model should incorporate these generic features, which are shown above to give rise to the fracture toughness master curve in Fig. 5.

Other physical effects that are already identified in our numerical solutions, such as the time evolution of the notch curvature $\rho(t)$ and the propagation of plastic yielding fronts, will be reported on separately, along with discussing the postcavitation dynamics. The latter are shown in Ref. [35] to lead to catastrophic failure, as we assume in this work, though we do not discuss them at all. More elaborate models and quantitative predictions will be explored in the future once additional experimental data become available.

A few important directions for future investigations emerge from the present analysis. Most notably, one would be interested in calculating the *intrinsic* toughness K_{Ic}, as opposed to the notch toughness K_Q, in the limit of $\rho \to 0$, where the notch or tip radius of curvature is not the dominant length scale in the problem. This touches upon a fundamental problem in glass physics, i.e., the existence of an intrinsic glassy length scale. Within the adopted nonequilibrium thermodynamic framework, such a length scale may appear in the macroscopic theory in an effective diffusion term proportional to $\nabla^2\chi$ in Eq. (4) [60,70]. This will be discussed in a separate report. Finally, it would be interesting to see whether variations in the glass composition, and their effect of the toughness, can be incorporated into the proposed theoretical framework [51].

ACKNOWLEDGMENTS

E. B. acknowledges support from the Israel Science Foundation (Grant No. 712/12), the Harold Perlman Family Foundation, and the William Z. and Eda Bess Novick Young Scientist Fund. C. H. R. is supported by the National Science Foundation under Grant No. DMR-1409560 and by the Applied Mathematics Program of the U.S. Department of Energy (DOE) Office of Advanced Scientific Computing Research under Contract No. DE-AC02-05CH11231.

[1] M. A. Meyers and K. K. Chawla, *Mechanical Behavior of Materials* (Cambridge University Press, Cambridge, England, 2009).
[2] J. J. Gilman, Mechanical behavior of metallic glasses, J. Appl. Phys. **46**, 1625 (1975).
[3] C. A. Schuh, T. C. Hufnagel, and U. Ramamurtny, Mechanical behavior of amorphous alloys, Acta Mater. **55**, 4067 (2007).
[4] M. Chen, Mechanical behavior of metallic glasses: Microscopic understanding of strength and ductility, Annu. Rev. Mater. Res. **38**, 445 (2008).
[5] W. H. Wang, Bulk metallic glasses with functional physical properties, Adv. Mater. **21**, 4524 (2009).
[6] M. M. Trexler and N. N. Thadhani, Mechanical properties of bulk metallic glasses, Prog. Mater. Sci. **55**, 759 (2010).
[7] Y. Q. Cheng and E. Ma, Atomic-level structure and structure-property relationship in metallic glasses, Prog. Mater. Sci. **56**, 379 (2011).
[8] W. H. Wang, The elastic properties, elastic models and elastic perspectives of metallic glasses, Prog. Mater. Sci. **57**, 487 (2012).
[9] T. Egami, T. Iwashita, and W. Dmowski, Mechanical properties of metallic glasses, Metals and alloys **3**, 77 (2013).
[10] T. C. Hufnagel, C. A. Schuh, and M. L. Falk, Deformation of metallic glasses: Recent developments in theory, simulations, and experiments, Acta Mater. **109**, 375 (2016).
[11] F. Spaepen, A microscopic mechanism for steady state inhomogeneous flow in metallic glasses, Acta Metall. **25**, 407 (1977).
[12] A. S. Argon, Plastic deformation in metallic glasses, Acta Metall. **27**, 47 (1979).

[13] M. L. Falk and J. S. Langer, Dynamics of viscoplastic deformation in amorphous solids, Phys. Rev. E **57**, 7192 (1998).

[14] L. C. E. Struik, *Physical Aging in Amorphous Polymers and Other Materials* (Elsevier, Amsterdam, 1978).

[15] M. D. Ediger, C. A. Angell, and S. R. Nagel, Supercooled liquids and glasses, J. Phys. Chem. **100**, 13200 (1996).

[16] A. L. Greer, Metallic glasses, Science **267**, 1947 (1995).

[17] A. Inoue, Stabilization of metallic supercooled liquid and bulk amorphous alloys, Acta Mater. **48**, 279 (2000).

[18] W. L. Johnson, Bulk amorphous metal—An emerging engineering material, JOM **54**, 40 (2002).

[19] J. F. Löffler, Bulk metallic glasses, Intermetallics **11**, 529 (2003).

[20] W. H. Wang, C. Dong, and C. H. Shek, Bulk metallic glasses, Mater. Sci. Eng. R **44**, 45 (2004).

[21] M. F. Ashby and A. L. Greer, Metallic glasses as structural materials, Scr. Mater. **54**, 321 (2006).

[22] J. Schroers, Bulk metallic glasses, Phys. Today **66**, No. 2, 32 (2013).

[23] J. J. Lewandowski, Effects of annealing and changes in stress state on fracture toughness of bulk metallic glass, Mater. Trans., JIM **42**, 633 (2001).

[24] J. J. Lewandowski, W. H. Wang, and A. L. Greer, Intrinsic plasticity or brittleness of metallic glasses, Philos. Mag. Lett. **85**, 77 (2005).

[25] P. Lowhaphandu and J. J. Lewandowski, Fracture toughness and notched toughness of bulk amorphous alloy: Zr-Ti-Ni-Cu-Be, Scr. Mater. **38**, 1811 (1998).

[26] M. D. Demetriou, M. E. Laubey, G. Garrett, J. P. Schramm, D. C. Hofmann, W. L. Johnson, and R. O. Ritchie, A damage-tolerant glass, Nat. Mater. **10**, 123 (2011).

[27] K. M. Flores and R. H. Dauskardt, Crack-tip plasticity in bulk metallic glasses, Mater. Sci. Eng. A **319–321**, 511 (2001).

[28] K. Fujita, A. Okamoto, N. Nishiyama, Y. Yokohama, H. Kimura, and A. Inoue, Effects of loading rates, notch root radius and specimen thickness on fracture toughness in bulk metallic glasses, J. Alloys Compd. **434–435**, 22 (2007).

[29] J. J. Lewandowski, M. Shazly, and A. Shamimi Nouri, Intrinsic and extrinsic toughening of metallic glasses, Scr. Mater. **54**, 337 (2006).

[30] P. Tandaiya, R. Narasimhan, and U. Ramamurty, Mode I crack tip fields in amorphous materials with application to metallic glasses, Acta Mater. **55**, 6541 (2007).

[31] J. Xu, U. Ramamurty, and E. Ma, The fracture toughness of bulk metallic glasses, JOM **62**, 10 (2010).

[32] D. L. Henan and L. Anand, Fracture of metallic glasses at notches: Effects of notch-root radius and the ratio of the elastic shear modulus to the bulk modulus on toughness, Acta Mater. **57**, 6057 (2009).

[33] P. Tandaiya, U. Ramamurty, and R. Narasimhan, Mixed mode (I and II) crack tip fields in bulk metallic glasses, J. Mech. Phys. Solids **57**, 1880 (2009).

[34] R. Narasimhan, H. Y. Subramanya, S. D. Patil, P. Tandaiya, and U. Ramamurty, Stationary crack tip fields in elastic-plastic solids: An overview of recent numerical simulations, J. Phys. D **42**, 214005 (2009).

[35] C. H. Rycroft and E. Bouchbinder, Fracture Toughness of Metallic Glasses: Annealing-Induced Embrittlement, Phys. Rev. Lett. **109**, 194301 (2012).

[36] R. Narasimhan, P. Tandaiya, I. Singh, R. L. Narayan, and U. Ramamurty, Fracture in metallic glasses: Mechanics and mechanisms, Int. J. Fract. **191**, 53 (2015).

[37] B. A. Sun and W. H. Wang, The fracture of bulk metallic glasses, Prog. Mater. Sci. **74**, 211 (2015).

[38] W. Li, Y. Gao, and H. Bei, On the correlation between microscopic structural heterogeneity and embrittlement behavior in metallic glasses, Sci. Rep. **5**, 14786 (2015).

[39] B. Ding, X. Li, X. Zhang, H. Wu, Z. Xu, and H. Gao, Brittle versus ductile fracture mechanism transition in amorphous lithiated silicon: From intrinsic nanoscale cavitation to shear banding, Nano Energy **18**, 89 (2015).

[40] K. M. Flores and R. H. Dauskardt, Mean stress effects on flow localization and failure in a bulk metallic glass, Acta Mater. **49**, 2527 (2001).

[41] E. Bouchaud, D. Boivin, J.-L. Pouchou, D. Bonamy, B. Poon, and G. Ravichandran, Fracture through cavitation in a metallic glass, Europhys. Lett. **83**, 66006 (2008).

[42] M. Q. Jiang, Z. Ling, J. X. Meng, and L. H. Dai, Energy dissipation in fracture of bulk metallic glasses via inherent competition between local softening and quasi-cleavage, Philos. Mag. **88**, 407 (2008).

[43] E. Bouchbinder, T. S. Lo, and I. Procaccia, Dynamic failure in amorphous solids via a cavitation instability, Phys. Rev. E **77**, 025101 (2008).

[44] E. Bouchbinder, T. S. Lo, I. Procaccia, and E. Shtilerman, Stability of an expanding circular cavity and the failure of amorphous solids, Phys. Rev. E **78**, 026124 (2008).

[45] P. Murali, T. G. Guo, Y. W. Zhang, R. Narasimhan, Y. Li, and H. J. Gao, Atomic Scale Fluctuations Govern Brittle Fracture and Cavitation Behavior in Metallic Glasses, Phys. Rev. Lett. **107**, 215501 (2011).

[46] Q. An, G. Garrett, K. Samwer, Y. Liu, S. V. Zybin, S. N. Luo, M. D. Demetriou, W. L. Johnson, and W. A. Goddard, Atomistic characterization of stochastic cavitation of a binary metallic liquid under negative pressure, J. Phys. Chem. Lett. **2**, 1320 (2011).

[47] P. Guan, S. Lu, M. J. B. Spector, P. K. Valavala, and M. L. Falk, Cavitation in Amorphous Solids, Phys. Rev. Lett. **110**, 185502 (2013).

[48] I. Singh, T. F. Guo, R. Narasimhan, and Y. W. Zhang, Cavitation in brittle metallic glasses—Effects of stress state and distributed weak zones, Int. J. Solids Struct. **51**, 4373 (2014).

[49] R. Maaß, P. Birckigt, C. Borchers, K. Samwer, and C. A. Volkert, Long range stress fields and cavitation along a shear band in a metallic glass: The local origin of fracture, Acta Mater. **98**, 94 (2015).

[50] R. Raghavan, P. Murali, and U. Ramamurty, On factors influencing the ductile-to-brittle transition in a bulk metallic glass, Acta Mater. **57**, 3332 (2009).

[51] G. Kumar, P. Neibecker, Y. H. Liu, and J. Schroers, Critical fictive temperature for plasticity in metallic glasses, Nat. Commun. **4**, 1536 (2013).

[52] M. Wakeda, J. Saida, J. Li, and S. Ogata, Controlled rejuvenation of amorphous metals with thermal processing, Sci. Rep. **5**, 10545 (2015).

[53] S. V. Madge, Toughness of bulk metallic glasses, Metals and alloys **5**, 1279 (2015).

[54] P. H. Sung and T. C. Chen, Effects of quenching rate on crack propagation in NiAl alloy using molecular dynamics, Comput. Mater. Sci. **114**, 13 (2016).
[55] C. H. Rycroft, Y. Sui, and E. Bouchbinder, An Eulerian projection method for quasi-static elastoplasticity, J. Comput. Phys. **300**, 136 (2015).
[56] A similar idea was first discussed in the context of annealing-induced ductile-to-brittle (embrittlement) transitions in Ref. [35] and later in the context of necking instabilities in soft glasses in D. M. Hoyle and S. M. Fielding, Age-Dependent Modes of Extensional Necking Instability in Soft Glassy Materials, Phys. Rev. Lett. **114**, 158301 (2015).
[57] J. S. Langer, Dynamics of shear-transformation zones in amorphous plasticity: Formulation in terms of an effective disorder temperature, Phys. Rev. E **70**, 041502 (2004).
[58] E. Bouchbinder, J. S. Langer, and I. Procaccia, Athermal shear-transformation theory of amorphous plastic deformation. I. Basic principles, Phys. Rev. E **75**, 036107 (2007).
[59] E. Bouchbinder, J. S. Langer, and I. Procaccia, Athermal shear-transformation-zone theory of amorphous plastic deformation. II. Analysis of simulated amorphous silicon, Phys. Rev. E **75**, 036108 (2007).
[60] M. L. Manning, J. S. Langer, and J. M. Carlson, Strain localization in a shear transformation zone model for amorphous solids, Phys. Rev. E **76**, 056106 (2007).
[61] J. S. Langer, Shear-transformation-zone theory of plastic deformation near the glass transition, Phys. Rev. E **77**, 021502 (2008).
[62] E. Bouchbinder and J. S. Langer, Nonequilibrium thermodynamics of driven amorphous materials. I. Internal degrees of freedom and volume deformation, Phys. Rev. E **80**, 031131 (2009).
[63] E. Bouchbinder and J. S. Langer, Nonequilibrium thermodynamics of driven amorphous materials. II. Effective-temperature theory, Phys. Rev. E **80**, 031132 (2009).
[64] E. Bouchbinder and J. S. Langer, Nonequilibrium thermodynamics of driven amorphous materials. III. Shear-transformation-zone plasticity, Phys. Rev. E **80**, 031133 (2009).
[65] M. L. Manning, E. G. Daub, J. S. Langer, and J. M. Carlson, Rate-dependent shear bands in a shear-transformation-zone model of amorphous solids, Phys. Rev. E **79**, 016110 (2009).
[66] M. L. Falk and J. S. Langer, Deformation and failure of amorphous, solid-like materials, Annu. Rev. Condens. Matter Phys. **2**, 353 (2011).
[67] E. Bouchbinder and J. S. Langer, Linear Response Theory for Hard and Soft Glassy Materials, Phys. Rev. Lett. **106**, 148301 (2011).
[68] C. H. Rycroft and F. Gibou, Simulations of a stretching bar using a plasticity model from the shear transformation zone theory, J. Comput. Phys. **231**, 2155 (2012).
[69] N. Perchikov and E. Bouchbinder, Variable-amplitude oscillatory shear response of amorphous materials, Phys. Rev. E **89**, 062307 (2014).
[70] K. Kamrin and E. Bouchbinder, Two-temperature continuum thermomechanics of deforming amorphous solids, J. Mech. Phys. Solids **73**, 269 (2014).
[71] K. B. Broberg, *Cracks and Fracture* (Academic, San Diego, 1999).